

Geophysical Research Letters[®]



RESEARCH LETTER

10.1029/2023GL102978

Projected West Antarctic Ocean Warming Caused by an Expansion of the Ross Gyre

Felipe Gómez-Valdivia¹ , Paul R. Holland¹ , Antony Siahhaan¹, Pierre Dutrieux¹ , and Emma Young¹

¹British Antarctic Survey, Cambridge, UK

Key Points:

- The UK Earth System Model produces a fairly realistic depiction of ocean conditions in West Antarctica
- Future projections suggest a rapid warming of the Amundsen Sea induced by a Ross Gyre (RG) expansion that is independent of forcing scenario
- The RG expansion is primarily caused by a surface stress curl intensification induced by anthropogenic trends in Antarctic sea ice

Supporting Information:

Supporting Information may be found in the online version of this article.

Correspondence to:

F. Gómez-Valdivia,
felmez@bas.ac.uk

Citation:

Gómez-Valdivia, F., Holland, P. R., Siahhaan, A., Dutrieux, P., & Young, E. (2023). Projected West Antarctic ocean warming caused by an expansion of the Ross Gyre. *Geophysical Research Letters*, 50, e2023GL102978. <https://doi.org/10.1029/2023GL102978>

Received 21 JAN 2023
Accepted 8 MAR 2023

Correction added on 5 APR 2024, after first online publication: The copyright line was changed.

© 2023. The Authors.

This is an open access article under the terms of the [Creative Commons Attribution License](https://creativecommons.org/licenses/by/4.0/), which permits use, distribution and reproduction in any medium, provided the original work is properly cited.

Abstract We use United Kingdom Earth System Model simulations from the Coupled Model Intercomparison Project 6 to analyze the Ross Gyre (RG) dynamics during the historical 1850–2014 period and under two contrasting future climate-change scenarios. The modeled RG is relatively stable, with an extent and strength that agree with observations. The projections exhibit an eastward gyre expansion into the Amundsen-Bellingshausen Seas that starts during the 2040s. The associated cyclonic ocean circulation enhances the onshore transport of warm Circumpolar Deep Water into the inner regional shelf, a regime change that increases the local subsurface shelf temperatures by up to 1.2°C and is independent of future forcing scenario. The RG expansion is generated by a regional ocean surface stress curl intensification associated with anthropogenic sea ice loss. If realised in reality, such a warming would strongly influence the future stability of the West Antarctic Ice Sheet.

Plain Language Summary We use a climate model to analyze ocean changes around West Antarctica. Our results reveal a human-driven ocean warming that increases the continental shelf temperature in the Amundsen-Bellingshausen Seas by more than 1°C in only ~30 years. This rapid warming is caused by the expansion of the Ross Gyre (RG), a large oceanic circulation in the region. The West Antarctic Ice Sheet is losing mass, causing sea-level rise, with the most rapid ice losses occurring in the Amundsen-Bellingshausen Seas. Our results suggest that an expansion of the RG could provide a mechanism whereby melt rates increase far beyond the current range. This could have an important influence on the sea-level rise caused by this region, with global impacts.

1. Introduction

The cyclonic Ross Gyre (RG) occupies the south-west Pacific sector of the Southern Ocean (Figure 1a). Evidence from hydrographic data (Gouretski, 1999), satellite altimetry (Dotto et al., 2018), and modeling (Rickard et al., 2010) suggests the RG extends more than 3,000 m below the ocean surface, with a transport of ~20 Sv, dominating the large-scale thermohaline structure of the Ross Sea (RS). The horizontal RG extent is limited by the continental shelf break to the south and the Pacific-Antarctic Ridge (PAR) to the north and west (Figure 1a). The southward-flowing eastern limb of the RG is much less strongly constrained by topography (Patmore et al., 2019) and its location is more variable (Dotto et al., 2018; Sokolov & Rintoul, 2009). The eastern RG limb, and the adjacent Antarctic Circumpolar Current (ACC), supply warm Circumpolar Deep Water (CDW) to the Amundsen Sea (AS) shelf (Jenkins et al., 2016; Nakayama et al., 2018) that supports rapid melting when it reaches ice shelf cavities. Increases in such ocean-driven melting are known to be causing thinning of the ice sheet in the nearby Amundsen-Bellingshausen Seas (Depoorter et al., 2013; Jenkins et al., 2016).

Satellite altimetry reveals variability in the RG strength and the eastern RG boundary position (Armitage et al., 2018; Dotto et al., 2018; Sokolov & Rintoul, 2009); whereas, numerical experiments have shown that the RG variability influences the water masses along the AS shelf (Nakayama et al., 2018). Any changes in the circulation of this region may be of wide importance, considering the ocean-driven ice loss from West Antarctica during recent decades (Paolo et al., 2015) and the consequences for global sea-level rise (Shepherd et al., 2018).

We use numerical simulations of the United Kingdom Earth System Model (UKESM1) implementation for the Coupled Model Intercomparison Project 6 (CMIP6) (Sellar et al., 2020) to analyze the RG dynamics and its effects on the Amundsen and Bellingshausen seas. We consider historical simulations and two contrasting future climate scenarios associated with the Shared Socioeconomic Pathways SSP1-1.9 and SSP5-8.5 (Riahi et al., 2017).

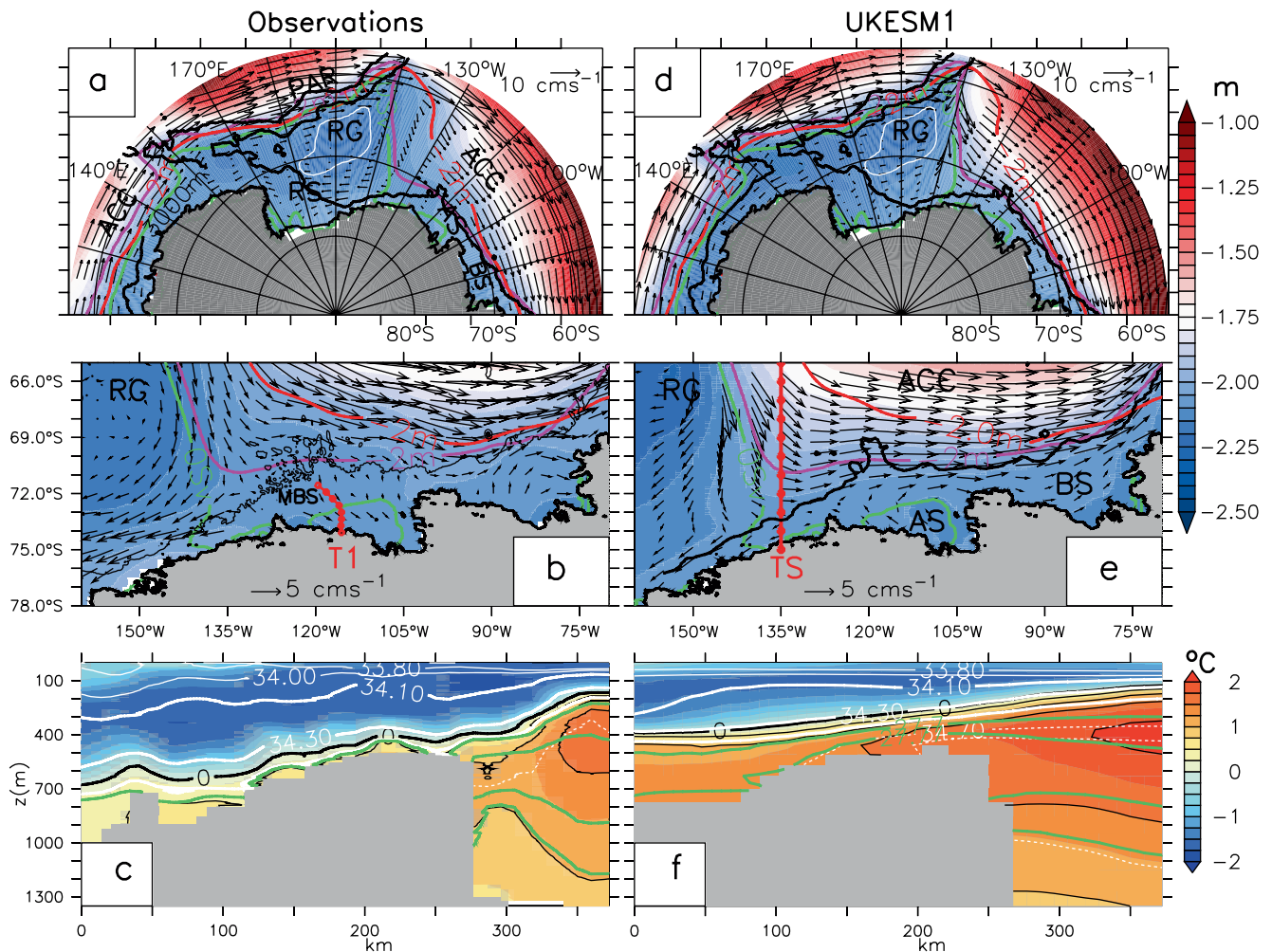


Figure 1. (a) Mean satellite Dynamic Ocean Topography [m] and derived surface geostrophic currents [cm s^{-1}] in the South Pacific. The mean satellite DOT_2 is in red and the ensemble-means of modeled BSF_0 and DOT_2 are shown in green and magenta, respectively. The 3,000 m isobath from ETOPO1 is in black, and the white line delimits the mean modeled RG core. (b) Same as panel (a), but for the Amundsen-Bellinghousen seas region, transect T1 is also shown. (c) The averaged austral-summer thermohaline structure in the upper 1,300 m along transect T1 from CTD data. Potential temperature [$^{\circ}\text{C}$] is shown in color and black contours, white contours exhibit isohalines [psu], green contours show the 27.7, 27.77, 27.81, and 27.82 potential density anomaly isopycnals [kg m^{-3}]. (d), (e), and (f) are equivalent to (a), (b) and (c), respectively, but for the modeled ensemble means and the model's 3,000 m isobath. Transect TS is shown in panel (e). The locations of the Ross Gyre (RG), Ross Sea (RS), Pacific-Antarctic Ridge (PAR), Amundsen Sea (AS), Bellinghousen Sea (BS), Marie Byrd Seamounts (MBS), and the Antarctic Circumpolar Current (ACC) are shown.

The following section describes the UKESM1 simulations and observations that support our research. Then, we consider how well modeling results match the observations. Next, we describe the historical and future RG evolution. Finally, we discuss the implications of the RG expansion for ocean conditions and ice-sheet melting in the AS.

2. Methods

UKESM1 is based on the HadGEM3-GC3.1 physical climate model (Kuhlbrodt et al., 2018) that simulates the coupled dynamics between land, atmosphere, ocean, and sea ice. Additionally, UKESM1 includes biogeochemical marine-terrestrial cycles, land-use management, and atmospheric chemistry (Sellar et al., 2019, 2020). The model variant UKESM1.1 includes an improved SO_2 parameterization (Hardacre et al., 2021) and produces a more realistic, up to $\sim 1^{\circ}\text{C}$ warmer, surface averaged temperature in the extratropical Northern Hemisphere (UKESM, 2022). The averaged Southern Hemisphere surface temperature differences between UKESM1 and UKESM1.1 are, however, less than $\sim 0.1^{\circ}\text{C}$ (UKESM, 2022); so UKESM1 simulations are sufficient for our

purposes. A second model variant UKESM1.0-ice has generated climate projections with an active Antarctic Ice Sheet model (Siahaan et al., 2021). However, UKESM1.0-ice has not been used to produce the historical (1850–2014) period because the ice sheet model needs to be initialized in the present day (Siahaan et al., 2021). An analysis of the historical RG evolution is a key feature of our study, and so we focus solely on UKESM1 simulations. These simulations have a relatively coarse resolution (1° ocean model) because higher-resolution UK climate models have substantial biases in the Southern Ocean (Andrews et al., 2020).

Under the SSP1-1.9 and the SSP5-8.5 scenarios, anthropogenic radiative forcing increases to $\sim 3.0 \text{ W m}^{-2}$ by the 2030s (O'Neill et al., 2016); subsequently, due to strong emissions mitigation, the radiative forcing in SSP1-1.9 progressively decreases to only 1.9 W m^{-2} in 2100. By contrast, the SSP5-8.5 scenario is based on intensive fossil-fuel energy consumption and the anthropogenic radiative forcing increases to 8.5 W m^{-2} in 2100 (O'Neill et al., 2016). We report ensembles of five 2015–2100 climate projections, preceded by five historical 1850–2014 simulations that follow on from the millennial preindustrial piControl experiment (Sellar et al., 2020).

We use the previously reported 2011–2016 Dynamic Ocean Topography (DOT) data set from Cryosat-2 satellite data (Naveira Garabato et al., 2019) to evaluate the UKESM1 ocean surface geostrophic circulation. We subtracted 0.3 m from the modeled Sea Surface Height (SSH) to generate a modeled DOT for comparison. This correction is the mean difference between the satellite DOT and the modeled SSH within the RG core, defined as the area delimited by the 15 Sv transport contour from the Barotropic Stream Function (BSF) (Figure 1a). The 0 Sv transport contour (BSF_0) is used to identify the horizontal RG extent. DOT_2 indicates the -2 m DOT contour, previously associated with the surface signature of the southern ACC boundary (Armitage et al., 2018; Dotto et al., 2018; Naveira Garabato et al., 2019).

We use two data sets to evaluate the modeled thermohaline structure. For the deep ocean and RG, we use long-term 1955–2017 averages from the World Ocean Atlas (WOA) (2018) database (Garcia et al., 2019). For the AS shelf, we use long-term 1994–2018 averages of Austral-summer CTD observations (Dutrieux et al., 2014; Jacobs et al., 2011; Jenkins et al., 2018; Kim et al., 2021) interpolated onto a three-dimensional grid with a meridional and zonal resolutions of 0.06° and 0.2° , respectively, and a vertical resolution of 1 m. We compare the ETOPO1 seabed topography (Amante & Eakins, 2009) with the model bathymetry.

3. Validation of the UKESM1 Dynamics

The modeled and satellite surface geostrophic circulation show a RG centered at $\sim 160^\circ\text{W}$ and bordered by an ACC with geostrophic surface currents exceeding 10 cms^{-1} (Figures 1a and 1d). The DOT_2 and BSF_0 contours are two measures of the horizontal RG extent, or equivalently the southern boundary of the ACC. West of 145°W these contours follow the PAR, illustrating how strongly the local bathymetry limits the RG extent (Figures 1a and 1d). The eastern RG boundary is far less constrained by bathymetry, with different direct hydrographic observations (Chu & Fan, 2007; Gouretski, 1999; Orsi et al., 1995) and altimetry (Armitage et al., 2018; Dotto et al., 2018) placing it at $\sim 140^\circ\text{W}$.

The modeled DOT_2 and BSF_0 exhibit a RG that, on average, extends to $\sim 140^\circ\text{W}$ during 2011–2016 (Figures 1d and 1e; magenta and green contours). The satellite DOT_2 and geostrophic circulation exhibit a surface RG expression extending to $\sim 135^\circ\text{W}$ during the same period (Figures 1a and 1b; red contour), suggesting that the modeled RG does not extend quite far enough eastward. This is confirmed by the WOA salinity distribution along section TS, at 135°W , which exhibits domed isohalines characteristic of the RG, while UKESM1 reproduces local tilted isohalines, characteristic of the ACC (Figure S1a in Supporting Information S1). The modeled eastern RG boundary is displaced westwards compared to observations during 2011–2016 and this is important to our conclusions, as discussed below. Nonetheless, during the millennial piControl and the 1850–2010 historical periods the eastward RG limb recurrently extends to 135°W (Figure S1b in Supporting Information S1). The RG strength and extent in UKESM1 are very realistic compared to several other climate models that have extreme biases in both features (Wang & Meredith, 2008).

Associated with the observed RG extension to $\sim 135^\circ\text{W}$ (Figure 1a), the altimetry circulation evidences a split of the RG southward flow near $\sim 69^\circ\text{S}$, apparently induced by the local bathymetry (Figure 1b). The westward branch of this bifurcation follows the cyclonic RG circulation, while the eastward branch follows the ACC to the east around the Marie Byrd Seamounts (MBS) (Figure 1b). The coarse UKESM1 bathymetry is smooth in this region (Figure 1e), and the modeled surface ACC flow is unaffected by the limited model's MBS representation.

The reproduced ACC flow reaches the shelf near 135°W, and dominates the surface shelf break circulation to the east (Figure 1e). This is in agreement with altimetry observations in the Bellingshausen Sea (BS), but not in the AS for this time period, as discussed below.

UKESM1 produces a cyclonic gyre, hereafter referred to as the Amundsen Shelf Gyre (ASG), that appears in the BSF and dominates the surface geostrophic circulation over the Amundsen shelf around ~110°W (Figure 1e). Several regional models have highlighted a cyclonic barotropic circulation in this region (e.g., Mathiot et al., 2017; Schodlok et al., 2012), though the details of the UKESM1 modeled circulation reflect the coarse resolution and smooth shelf bathymetry. Previous studies (e.g., Dutrieux et al., 2014; Thoma et al., 2008) have concluded that zonal winds along the Amundsen shelf break influence the ocean conditions on the AS shelf. In turn, local zonal winds are characterized by an energetic decadal variability and, an anthropogenic forced, centennial eastward trend of ~0.4 m s⁻¹ century⁻¹ (Holland et al., 2019, 2022). In response to eastward wind trends, regional high resolution ocean models reproduce a subsurface Amundsen shelf warming rate of 0.33°C century⁻¹, of which approximately half is anthropogenically forced (Naughten et al., 2022). In agreement, the shelf break UKESM1 winds along the AS depict a historical eastward wind trend and, as discussed below, UKESM1 produces a historical subsurface Amundsen shelf warming of ~0.12°C century⁻¹.

UKESM1's temperature biases are relatively modest along the Antarctic shelf (Purich & England, 2021). This is confirmed by the comparison between the observed and modeled thermohaline section along transect T1 (Figures 1c and 1f), at the Dotson Trough (Figure 1b). Model results and observations exhibit warm CDW on the shelf, overlain by Winter Water and Antarctic Surface Water. In agreement with observations, the modeled subsurface CDW layer thins toward the south, where the Antarctic Surface Water is prominent (Figures 1c and 1f). The properties of the modeled CDW are warmer and saltier and the modeled structure is smoother than observed (Figures 1c and 1f), but overall UKESM1 performs remarkably well considering its coarse resolution and smooth bathymetry, visible when comparing the 3,000 isobath in panels (b) and (e) of Figure 1. UKESM1 is also one of the CMIP6 models that better reproduces the spatial distribution of Antarctic Bottom Water (AABW) (Heuzé, 2021). Consequently, the modeled temperature along the southwestern RS, characterized by the presence of RS Bottom Water, agrees with observations (Figure S1c in Supporting Information S1).

The western shelf break circulation in the AS consists of a westward surface flow over an eastward undercurrent (Thompson et al., 2020; Walker et al., 2013); this baroclinic structure is reproduced by UKESM1 (Figure 2b), despite its coarse resolution.

4. Climatic Changes Within the UKESM1 Simulations

In the historical simulations, the decadal-averaged BSF₀ implies a modeled RG that extends eastward to ~130°W during the 1980s, before retreating to ~140°W by the 2010s (Figure 2a). Along the shelf-break, the westward barotropic flow within the RG weakens by the 2010s, while the eastward circulation outside the RG strengthens, with barotropic shelf currents exceeding 3 cms⁻¹ along the Amundsen-Bellingshausen seas (Figure 2a). On-shelf, the cyclonic ASG dominates the barotropic circulation throughout the 1980s–2010s period (Figure 2a).

In the SSP1-1.9 projections, the BSF₀ contour reveals an interaction between the RG and the ASG that initiates during the 2040s (Figure 2a). During this decade, the BSF₀ suggests the development of a cyclonic gyre on the BS shelf, hereafter referred to as the Bellingshausen Shelf Gyre (BSG), centered at ~85°W (Figure 2a).

By the 2070s, the interaction between the RG, the ASG, and the BSG, induces an overall cyclonic circulation characterized by the eastward RG expansion into the Amundsen and Bellingshausen seas (Figure 2a). The barotropic shelf flow are stronger and include a quasi-continuous westward inner-shelf current that reaches a decadal averaged magnitude larger than 2 cms⁻¹ (Figure 2a).

The evolution of zonal velocity along the transect T2, at the western AS shelf break, reflects the modeled RG changes. Before the 2000s, the modeled shelf break circulation includes the westward Antarctic Slope Current flowing above an eastward undercurrent (Figure 2b). By the 2010s, the RG retreats westward to ~140°W and a strengthened ACC induces a dominant barotropic eastward flow over the shelf break (Figure 2a). The baroclinicity does not change substantially, so the maximum eastward flow is at depth (Figure 2b) reaching up to 3 cms⁻¹ at ~500 m.

After the 2040s, the RG expansion into the AS commences (Figure 2a). The eastward barotropic flow first weakens, before changing westward during the 2050s–2060s (Figure 2b). By the 2070s the local shelf break circulation

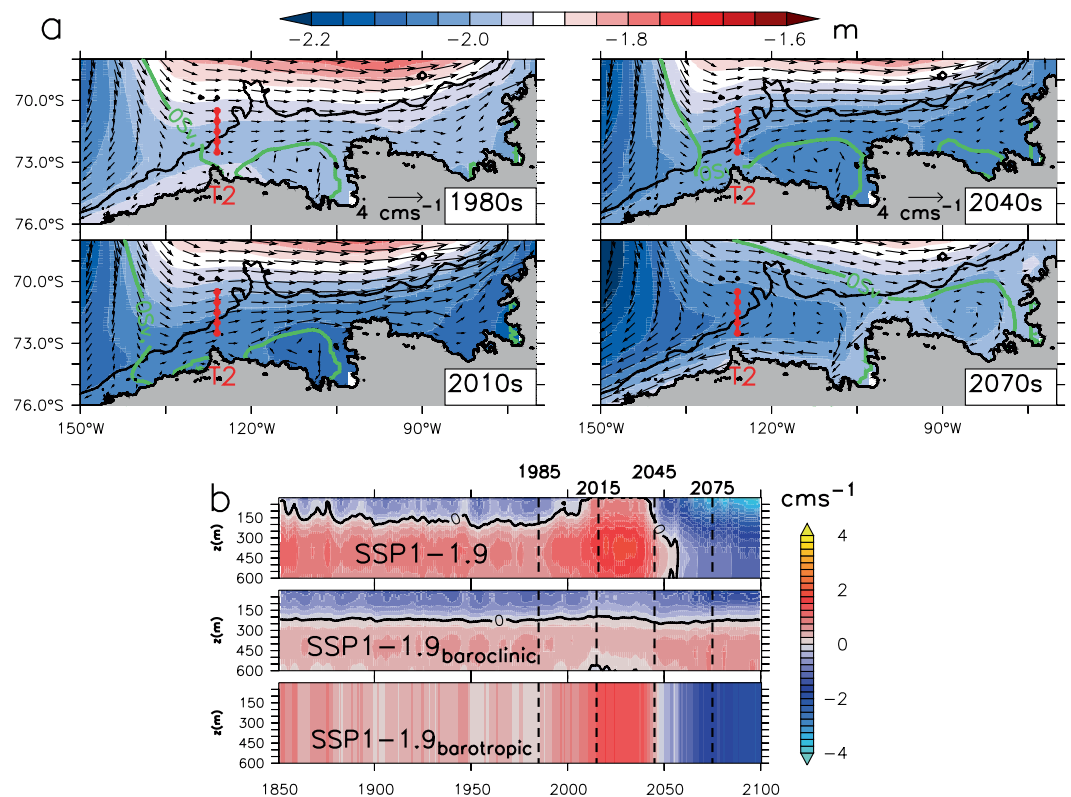


Figure 2. (a) Decadal averages of historical and SSP1-1.9 ensemble-mean Dynamic Ocean Topography [m] and barotropic flow [cms⁻¹] during the 1980s, 2010s, 2040s, and 2070s; the transect T2, at 125°W, is also shown. (b) Hovmöller diagram of the ensemble-mean meridionally-averaged zonal velocity at transect T2 from historical and SSP1-1.9 simulations; the barotropic and baroclinic components are shown. The vertical dashed lines indicate the middle year of the decades 1980s, 2010s, 2040s, and 2070s. The SSP5-8.5 ensemble-mean exhibits a more energetic Ross Gyre extent into the Amundsen-Bellingshausen Seas that induces a stronger dominant cyclonic circulation (Figure S2 in Supporting Information S1).

becomes entirely westward, strongest at the surface due to the persistent baroclinic component (Figure 2b) associated with the effects of the cyclonic circulation on the subsurface isopycnals. There is a small projected increase in baroclinicity, but the dominant changes are barotropic.

The circulation of the Amundsen-Bellingshausen Seas is mainly driven by the cyclonic atmospheric AS Low (Raphael et al., 2016; Turner et al., 2013), which comprises westerlies to the north and coastal easterlies to the south. Accordingly, the UKESM1 reproduces a preferentially cyclonic regional surface stress (Figure 3a).

The decadal averaged ocean surface stress during the 2010s and the 2070s reveals a cyclonic intensification in the projections (Figure 3a). The associated cyclonic Ocean Surface Stress Curl (OSC) strengthening explains the RG expansion into the Amundsen-Bellingshausen Seas, where the OSC intensification is stronger (Figure 3a). The integrated OSC over the dynamic RG domain located east of 170°W, hereafter referred as ROSC, gradually amplifies after the 2020s and by the early 2050s reaches a similar ensemble-average of $\sim 3.5 \times 10^5 \text{ N m}^{-1}$ under both scenarios (Figure 3b). Subsequently, under SSP1-1.9 the RG domain slightly grows, and the ROSC modestly strengthens to $\sim 4.5 \times 10^5 \text{ N m}^{-1}$ by 2100; under SSP5-8.5 the ROSC strengthens further to reach $\sim 6.5 \times 10^5 \text{ N m}^{-1}$ in 2100 (Figure 3b).

The Barotropic Kinetic Energy (BKE) per unit mass is defined as:

$$\frac{u_{bar}^2 + v_{bar}^2}{2}$$

where u_{bar} and v_{bar} are the depth-averaged barotropic ocean velocity components. The integrated BKE over the RG domain located east of 170°W, hereafter RBKE, reflects the OSC effect on the RG. The RBKE variability

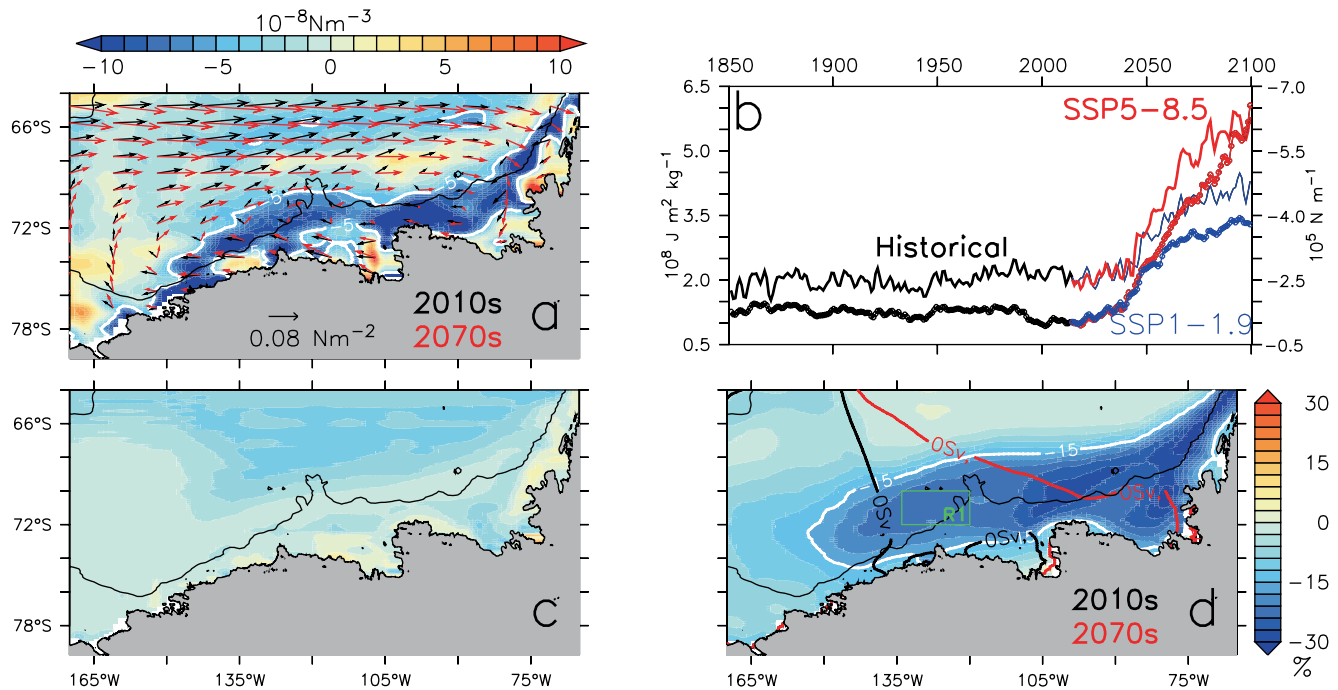


Figure 3. (a) Difference of the ensemble-mean Ocean Surface Stress Curl (OSC) between the 2070s and the 2010s, overlain by the averaged ensemble-mean surface stress during the 2010s (black) and the 2070s (red). White contours delimit regions with strong cyclonic OSC intensification ($>5 \times 10^{-8} \text{ Nm}^{-3}$) throughout the 60-year period. (b) The ensemble-mean ROSC [Nm^{-1}] and the ensemble-mean RBKE [$\text{Jm}^2 \text{ kg}^{-1}$] are both shown by continuous lines and by lines-and-dots, respectively. Difference of the ensemble-mean wind-only stress curl [Nm^{-3}] (c) and the ensemble-mean sea ice concentration [%] (d) between the 2070s and the 2010s. The white contour in panel (d) surrounds the domain where the sea ice concentration decreases more than 15% between the 2010s and the 2070s; accordingly, the projected OSC intensification in region R1 is dominated by the Ice-only Stress Curl component (Figure S4 in Supporting Information S1). Averaged ensemble-mean Ross Gyre extent during both decades are shown by black and red contours, respectively. Panels (a), (c), and (d), show SSP1-1.9 ensemble results.

is explained by the ROSC (Figure 3b), especially after the 2040s–2050s, when the RG extension into the Amundsen-Bellinghousen Seas occurs (Figure 2a). Correlation analysis reveals a RBKE that follows the ROSC with a 0–1 month lag, in agreement with the expected rapid ocean barotropic response to surface stress forcing (Gill, 1982). The ROSC effect on the RBKE is evident in each ensemble member under both SSP scenarios (Figure S3 in Supporting Information S1).

The ocean surface stress ($\vec{\tau}$) is the sum of the air-ocean stress ($\vec{\tau}_{AO}$) and the ice-ocean stresses ($\vec{\tau}_{IO}$) weighted by the sea ice concentration (α):

$$\vec{\tau} = (1 - \alpha)\vec{\tau}_{AO} + \alpha\vec{\tau}_{IO} \quad (1)$$

In agreement with reported observations (Dotto et al., 2018; Holland et al., 2019), along the Amundsen-Bellinghousen seas the ocean surface velocity reproduced by UKESM is much weaker than the reproduced near-surface wind velocity. Thus, the air-ocean stress, can be expressed as:

$$\vec{\tau}_{AO} = \rho_{air} C_d |\vec{U}_{10}| \vec{U}_{10}$$

$\rho_{air} = 1.25 \text{ kg m}^{-3}$ is the air density. $C_d = 1.25 \times 10^{-3}$ is the air-water drag coefficient. \vec{U}_{10} and α are, respectively, the modeled 10 m wind velocity and modeled sea ice concentration. Hereafter, we define the weighted components in the left side of Equation 1 as the wind-only stress and the ice-only stress, respectively.

The offshore wind-only stress curl (WSC) intensification helps to explain the offshore OSC strengthening, especially around 120°W (Figures 3a and 3c). Along the regional shelf, however, the WSC has little influence on the local OSC intensification (Figures 3a and 3c) and the latter is better explained by the loss of sea ice (Figures 3a and 3d), through the energetic Ice-only Stress Curl induced by the increased sea-ice mobility at lower concentrations. In agreement with the projected rapid Antarctic sea ice decline reproduced by different CMIP6 models

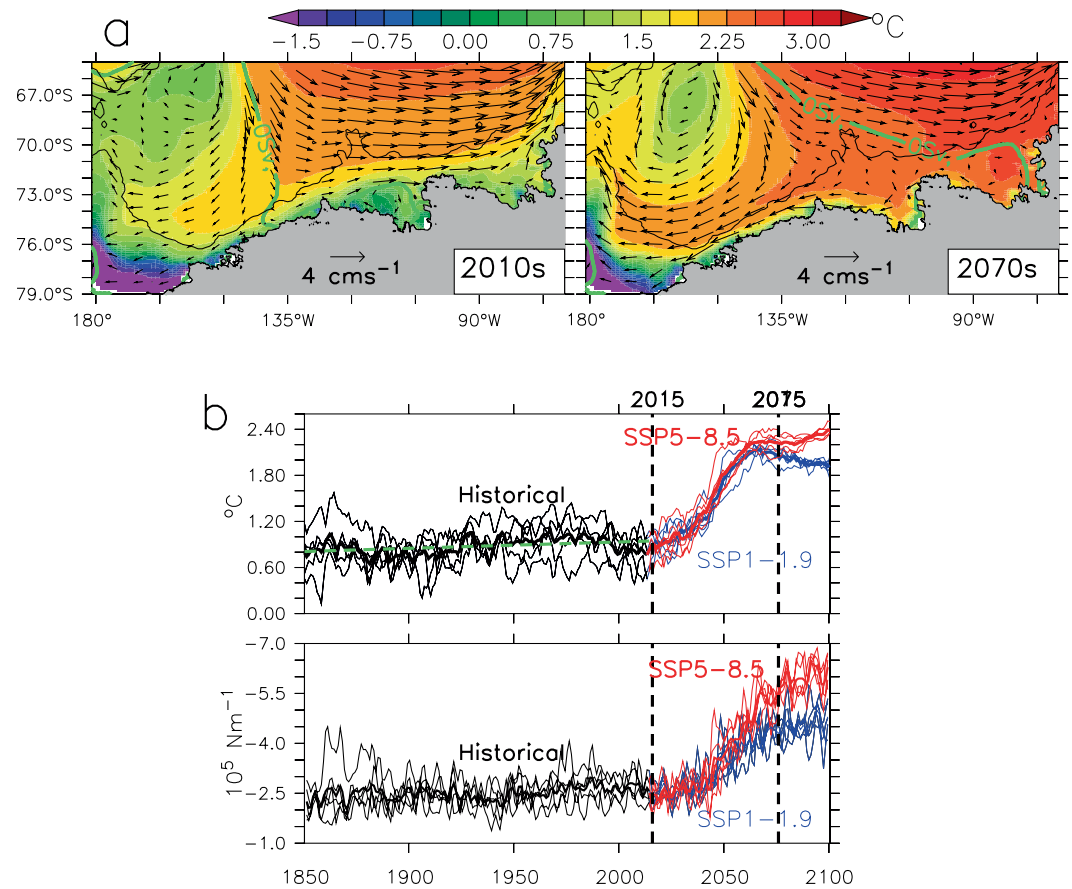


Figure 4. (a) Warming pattern induced by the Ross Gyre (RG) expansion under the SSP1-1.9 scenario. Decadal 2010s and 2070s averages of ensemble-mean subsurface potential temperature between 200 and 700 m depth overlain by the averaged ensemble-mean barotropic circulation and the averaged ensemble-mean RG extent (green contour). The 3,000 m isobath is shown for reference. (b) Time series of the RG's Ocean Surface Stress Curl and the mean potential temperature on the Amundsen Sea shelf (within the 3,000 m isobath, between 200 and 700 m depth, and between 115° and 100°W). Thin and thick lines correspond to ensemble members and ensemble means, respectively. The green dashed line in the temperature panel is the modeled $\sim 0.12^{\circ}\text{C century}^{-1}$ warming trend during the historical 1850–2014 period, similar to the warming trend reported by Naughten et al. (2022). For reference, the vertical dashed lines indicate the middle year of the 2010s and 2070s decades.

(Casagrande et al., 2023; Roach et al., 2020), under SSP1-1.9 the UKESM1 sea ice concentration along the regional shelf and shelf break decreases by more than 15% between the 2010s and 2070s (Figure 3d).

By the 2070s, the RG intrusion dominates the Amundsen-Bellinghousen Seas circulation, inducing a stronger advection of offshore CDW onto the regional shelf (Figure 4a). On the Amundsen and Bellinghousen continental shelves, the subsurface temperature warms by more than 1°C between the 2010s and the 2070s under SSP1-1.9 (Figure 4a), and this could have important implications for the stability of the West Antarctic Ice Sheet. The CDW advection extends into the RS (Figure 4a) and, although water colder than -1°C persists along the local inner shelf, the subsurface RS reaches $\sim 2^{\circ}\text{C}$ along the shelf-break during the 2070s (Figure 4a). As described below, the warming effect due to the RG expansion is stronger under the SSP5-8.5 scenario.

Between 115° and 100°W and south of the 3,000 m isobath the subsurface potential temperature increases from a 1850–2014 average of $\sim 0.8^{\circ}\text{C}$ to an average exceeding 2.0°C in the 2060s–2070s (Figure 4b). Subsequently, the SSP1-1.9 temperatures decreased to $\sim 1.9^{\circ}\text{C}$ by 2100; whereas, the SSP5-8.5 subsurface shelf temperature continues increasing to $\sim 2.3^{\circ}\text{C}$ by 2100. Comparison with the ROSC confirms that the energetic shelf warming along the AS, induced by the local RG intrusion (Figure 4a), is associated with the surface forcing that causes the RG expansion into the region (Figure 4b). The long-term subsurface shelf warming trend during the 1850–2014 period (Figure 4b), shown by the green dashed line, is not explained by the RG expansion, but by the previously

reported (Holland et al., 2019; Naughten et al., 2022) long-term eastward trend of the zonal wind along the AS shelf break.

5. Discussion

Previous studies describe decadal variability in the CDW transport into the AS, induced by atmospheric variability associated with the tropical Pacific (Jenkins et al., 2016, 2018; Thoma et al., 2008). In addition, Naughten et al. (2022) report a modeled wind-driven $\sim 0.33^{\circ}\text{C century}^{-1}$ subsurface AS warming during 1920–2020. In agreement with these findings, the UKESM1 historical subsurface shelf temperature exhibits a decadal variability superimposed upon a long-term $\sim 0.12^{\circ}\text{C century}^{-1}$ warming (Figure 4b). A much more rapid shelf warming is induced, however, by the enhanced CDW advection due to the eastward RG intrusion into the Amundsen-Bellingshausen Seas (Figures 4a and 4b). This represents an oceanic regime change that is completely outside the envelope of previously documented changes. The CDW advection also extends to the RS (Figure 4a) inducing a contraction of the local AABW. However, a detailed analysis of the AABW evolution under climate change scenarios is outside the scope of the present study.

The eastward RG intrusion to the Amundsen-Bellingshausen Seas is generated by the cyclonic OSC strengthening (Figure 3a), explained mainly by a projected rapid sea ice reduction that characterizes UKESM1 (Figure 3d) and several other CMIP6 models (Casagrande et al., 2023; Roach et al., 2020). The regional OSC derived from the SSP1-1.9 and SSP5-8.5 scenarios follow the associated anthropogenic radiative forcing shown in O'Neill et al. (2016, Figure 3). However, we caution that, like other CMIP6 models, UKESM1 has a higher Equilibrium Climate Sensitivity compared to previous climate model generations (Sellar et al., 2019), which may be unrealistic (Forster et al., 2020). In addition, CMIP6 simulations of Antarctic sea ice have some limitations (Casagrande et al., 2023; Roach et al., 2020; Shu et al., 2020), which suggest that the projected UKESM1 sea ice loss, and the associated OSC intensification over Western Antarctica, could be over-estimated. Recent observations show, however, an abrupt on-going Antarctic sea ice decline trend that started in the mid-2010s (Parkinson, 2019; Raphael & Hancock, 2022; Turner et al., 2017; Wang et al., 2019).

The SSP1-1.9 anthropogenic emissions mitigation effect is evident on the Amundsen-Bellingshausen Shelf dynamics after the ~ 2060 s, when the local sea ice loss stops and the local cyclonic OSC progressively becomes weaker (Figure S4 in Supporting Information S1). However, these changes manifest too late to avoid the RG intrusion into the Amundsen-Bellingshausen seas and the associated intense shelf warming (Figures 4a and 4b).

During the 1980s the RG extended eastward of $\sim 130^{\circ}\text{W}$ (Figure 2a) and the eastern RG limb enhanced the westward Antarctic Slope Current along transect T2 (Figure 2b). The dominance of the Antarctic Slope Current at T2 during 1850–2000 (Figure 2b) suggests that this RG extent was prevalent during this period. Subsequently, however, the eastern RG boundary retreated westward to $\sim 140^{\circ}\text{W}$ (Figure 2a) and the ACC extended to the shelf break, strengthening the local undercurrent at T2 (Figure 2b). The undercurrent intensification has been associated with the onshore CDW transport enhancement into the Amundsen shelf, which explains the increased ice shelf melting observed during recent decades (Naughten et al., 2022). Our results show that a stronger shelf warming could be generated in the future by the dominant cyclonic circulation associated with the reported RG expansion (Figure 4).

The altimetry-derived geostrophic circulation exhibits the splitting of the southward RG limb at $\sim 69^{\circ}\text{S}$ (Figure 1b), apparently generated by the local bathymetry. The westward branch of this flow follows the cyclonic RG, while the eastward branch continues as the ACC to the east around the MBS (Figure 1b). This is not reproduced by UKESM1, apparently due to the smooth model bathymetry and coarse resolution. The modeled shelf water mass distribution is broadly in agreement with the Conductivity Temperature Deep instrument (CTD) observations (Figures 1c and 1f), though the reproduced subsurface shelf water is, on average, warmer and saltier. Future research should focus on testing our findings within higher resolution models that better match the detailed oceanography and ice-shelf dynamics of this region.

6. Conclusions

We analyze the dynamics of the RG, West Antarctica, reproduced by the UK Earth System Model (UKESM1). We report, for the first time, a projected RG expansion into the Amundsen and Bellingshausen seas that characterizes

the 2040s–2050s modeled dynamics. The RG expansion is driven by the cyclonic OSC intensification, associated mainly with the projected loss of sea ice.

This RG expansion enhances the onshore transport of warm CDW into the AS, bringing much warmer CDW onto the shelf than is currently present. This increases the subsurface shelf temperature by more than $\sim 1^{\circ}\text{C}$ during the 2040–2070 period. This dramatic warming occurs irrespective of the anthropogenic forcing scenario and, if realised, would have drastic consequences for melting of the West Antarctic Ice Sheet. These simulated future ocean changes are completely outside the envelope of both observed historical variability and previously modeled and inferred trends.

The coarse UKESM1 climate model performs remarkably well in many aspects of the West Antarctica oceanography, though the modeled RG was slightly far west compared to 2011–2016 observations, and the flow lacks sensitivity to local bathymetric features. In addition, CMIP6 models, such as UKESM1, have some limitations in their representation of Antarctic sea ice; yet, the latest observations evidence an abrupt Antarctic sea ice decline trend that started in the mid-2010s. We cannot be sure when or if the RG intrusion into the Amundsen-Bellingshausen Seas, induced by the loss of sea ice, is likely to take place. However, if such a phenomenon were to occur it would be fundamental to the future stability of the West Antarctic Ice Sheet. Further research into the feasibility of this oceanic regime change is urgently required.

Data Availability Statement

The Met Office Hadley Centre (MOHC) offers access to the UKESM1 Pre-industrial MOHC (2019b), historical MOHC (2019a), SSP1-1.9 MOHC (2019d), and SSP5-8.5 MOHC (2019c) data, respectively. WOA and Cryosat-2 data are available at WOA (2018) and ESA (2022), respectively.

Acknowledgments

This work was partly funded by the National Environmental Research Council (NERC) national capability Grants for the UKESM project, NE/N017978/1 and NE/N01801X/1. This publication was supported by the PROTECT project. PROTECT has received funding from the European Union's Horizon 2020 research and innovation programme under Grant 869304, PROTECT contribution number 59. We thank Robin Smith, two anonymous reviewers, and the associate editor for their constructive comments on this research.

References

- Amante, C., & Eakins, B. (2009). *ETOPO1 1 Arc-Minute Global Relief Model: Procedures, data sources and analysis*. (Technical Report). NOAA National Geophysical Data Center. <https://doi.org/10.7289/V5C8276M>
- Andrews, M. B., Ridley, J. K., Wood, R. A., Andrews, T., Blockley, E. W., Booth, B., et al. (2020). Historical simulations with HadGEM3-GC3.1 for CMIP6. *Journal of Advances in Modeling Earth Systems*, 12(6), e2019MS001995. <https://doi.org/10.1029/2019MS001995>
- Armitage, T. W. K., Kwok, R., Thompson, A. F., & Cunningham, G. (2018). Dynamic topography and sea level anomalies of the Southern Ocean: Variability and teleconnections. *Journal of Geophysical Research: Oceans*, 123(1), 613–630. <https://doi.org/10.1002/2017JC013534>
- Casagrande, F., Stachelski, L., & Buss de Souza, R. (2023). Assessment of Antarctic sea ice area and concentration in CMIP5 and CMIP6 models. *International Journal of Climatology*. <https://doi.org/10.1002/joc.7916>
- Chu, P. C., & Fan, C. (2007). An inverse model for calculation of global volume transport from wind and hydrographic data. *Journal of Marine Systems*, 65(1), 376–399. <https://doi.org/10.1016/j.jmarsys.2005.06.010>
- Depoorter, M. A., Bamber, J. L., Griggs, J. A., Lenaerts, J. T. M., Ligtenberg, S. R. M., van den Broeke, M. R., & Moholdt, G. (2013). Calving fluxes and basal melt rates of Antarctic ice shelves. *Nature*, 502(7469), 89–92. <https://doi.org/10.1038/nature12567>
- Dotto, T. S., Naveira Garabato, A., Bacon, S., Tsamados, M., Holland, P. R., Hooley, J., et al. (2018). Variability of the Ross Gyre, Southern Ocean: Drivers and responses revealed by satellite altimetry. *Geophysical Research Letters*, 45(12), 6195–6204. <https://doi.org/10.1029/2018GL078607>
- Dutrieux, P., Rydt, J. D., Jenkins, A., Holland, P. R., Ha, H. K., Lee, S. H., et al. (2014). Strong sensitivity of Pine Island ice-shelf melting to climatic variability. *Science*, 343(6167), 174–178. <https://doi.org/10.1126/science.1244341>
- ESA. (2022). CryoSat products. [Dataset]. Earth Online. Retrieved from <https://earth.esa.int/eogateway/catalog/cryosat-products>
- Forster, P. M., Maycock, A. C., McKenna, C. M., & Smith, C. J. (2020). Latest climate models confirm need for urgent mitigation. *Nature Climate Change*, 10(1), 7–10. <https://doi.org/10.1038/s41558-019-0660-0>
- Garcia, H., Boyer, T. P., Locarnini, R. A., Mishonov, A., Grodsky, C., Weathers, K. A., et al. (2019). *World Ocean Atlas 2018: Product documentation*. (Technical Report). NOAA National Centers for Environmental Information.
- Gill, A. E. (1982). *Atmosphere-ocean dynamics*. Academic Press.
- Gouretski, V. (1999). The large-scale thermohaline structure of the Ross Gyre. In G. Manzella (Ed.), *Oceanography of the Toss Sea Antarctica*. Springer. https://doi.org/10.1007/978-88-470-2250-8_6
- Hardacre, C., Mulcahy, J. P., Pope, R. J., Jones, C. G., Rumbold, S. T., Li, C., et al. (2021). Evaluation of SO_2 , SO_4^{2-} and an updated SO_2 dry deposition parameterization in the United Kingdom Earth System Model. *Atmospheric Chemistry and Physics*, 21(24), 18465–18497. <https://doi.org/10.5194/acp-21-18465-2021>
- Heuzé, C. (2021). Antarctic bottom water and North Atlantic deep water in CMIP6 models. *Ocean Science*, 17(1), 59–90. <https://doi.org/10.5194/os-17-59-2021>
- Holland, P. R., Bracegirdle, T. J., Dutrieux, P., Jenkins, A., & Steig, E. J. (2019). West Antarctic ice loss influenced by internal climate variability and anthropogenic forcing. *Nature Geoscience*, 12(9), 718–724. <https://doi.org/10.1038/s41561-019-0420-9>
- Holland, P. R., O'Connor, G. K., Bracegirdle, T. J., Dutrieux, P., Naughten, K. A., Steig, E. J., et al. (2022). Anthropogenic and internal drivers of wind changes over the Amundsen Sea, West Antarctica, during the 20th and 21st centuries. *The Cryosphere*, 16(12), 5085–5105. <https://doi.org/10.5194/tc-16-5085-2022>
- Jacobs, S. S., Jenkins, A., Giulivi, C. F., & Dutrieux, P. (2011). Stronger ocean circulation and increased melting under Pine Island Glacier ice shelf. *Nature Geoscience*, 4(8), 519–523. <https://doi.org/10.1038/ngeo1188>
- Jenkins, A., Dutrieux, P., Jacobs, S., Steig, E. J., Gudmundsson, G. H., Smith, J., & Heywood, K. J. (2016). Decadal ocean forcing and Antarctic ice sheet response: Lessons from the Amundsen Sea. *Oceanography*, 29(4), 106–117. <https://doi.org/10.5670/oceanog.2016.103>

- Jenkins, A., Shoosmith, D., Dutrieux, P., Jacobs, S., Kim, T. W., Lee, S. H., et al. (2018). West Antarctic Ice Sheet retreat in the Amundsen Sea driven by decadal oceanic variability. *Nature Geoscience*, *11*, 733–738. <https://doi.org/10.1038/s41561-018-0207-4>
- Kim, T.-W., Yang, H. W., Dutrieux, P., Wählin, A. K., Jenkins, A., Kim, Y. G., et al. (2021). Interannual variation of modified circumpolar deep water in the Dotson-Getz Trough, West Antarctica. *Journal of Geophysical Research: Oceans*, *126*(12), e2021JC017491. <https://doi.org/10.1029/2021JC017491>
- Kuhlbrodt, T., Jones, C. G., Sellar, A., Storkey, D., Blockley, E., Stringer, M., et al. (2018). The low-resolution version of HadGEM3 GC3.1: Development and evaluation for global climate. *Journal of Advances in Modeling Earth Systems*, *10*(11), 2865–2888. <https://doi.org/10.1029/2018MS001370>
- Mathiot, P., Jenkins, A., Harris, C., & Madec, G. (2017). Explicit representation and parametrised impacts of under ice shelf seas in the Z* coordinate ocean model NEMO 3.6. *Geoscientific Model Development*, *10*(7), 2849–2874. <https://doi.org/10.5194/gmd-10-2849-2017>
- MOHC. (2019a). Met Office Hadley Centre (MOHC) UKESM1-0-LL model output for the “historical” experiment. [Dataset]. CEDA Archive, November 2019. Retrieved from <https://catalogue.ceda.ac.uk/uuid/59c10ac7bea2424f8eb64f0e310a2d4f>
- MOHC. (2019b). Met Office Hadley Centre (MOHC) UKESM1-0-LL model output for the “piControl” experiment. [Dataset]. CEDA Archive, November 2019. Retrieved from <https://catalogue.ceda.ac.uk/uuid/208e35d6d82444b18b1f3b938cdc080f>
- MOHC. (2019c). Met Office Hadley Centre (MOHC) UKESM1-0-LL model output for the “ssp585” experiment. [Dataset]. CEDA Archive, November 2019. Retrieved from <http://catalogue.ceda.ac.uk/uuid/dd5bd2e874a44a0db9b0757d633c212c>
- MOHC. (2019d). WCRP CMIP6: Met Office Hadley Centre (MOHC) UKESM1-0-LL model output for the “ssp119” experiment. [Dataset]. CEDA Archive, November 2019. Retrieved from <https://catalogue.ceda.ac.uk/uuid/7910bf8499c34c87a0bd4402402465a2>
- Nakayama, Y., Menemenlis, D., Zhang, H., Schodlok, M., & Rignot, E. (2018). Origin of Circumpolar Deep Water intruding onto the Amundsen and Bellingshausen Sea continental shelves. *Nature Communications*, *9*(1), 3403. <https://doi.org/10.1038/s41467-018-05813-1>
- Naughten, K. A., Holland, P. R., Dutrieux, P., Kimura, S., Bett, D. T., & Jenkins, A. (2022). Simulated twentieth-century ocean warming in the Amundsen Sea, West Antarctica. *Geophysical Research Letters*, *49*(5), e2021GL094566. <https://doi.org/10.1029/2021GL094566>
- Naveira Garabato, A. C., Dotto, T. S., Hooley, J., Bacon, S., Tsamados, M., Ridout, A., et al. (2019). Phased response of the subpolar Southern Ocean to changes in circumpolar winds. *Geophysical Research Letters*, *46*(11), 6024–6033. <https://doi.org/10.1029/2019GL082850>
- O’Neill, B. C., Tebaldi, C., van Vuuren, D. P., Eyring, V., Friedlingstein, P., Hurtt, G., et al. (2016). The scenario model intercomparison project (ScenarioMIP) for CMIP6. *Geoscientific Model Development*, *9*(9), 3461–3482. <https://doi.org/10.5194/gmd-9-3461-2016>
- Orsi, A. H., Whitworth, T., & Nowlin, W. D. (1995). On the meridional extent and fronts of the Antarctic Circumpolar Current. *Deep Sea Research Part I: Oceanographic Research Papers*, *42*(5), 641–673. [https://doi.org/10.1016/0967-0637\(95\)00021-w](https://doi.org/10.1016/0967-0637(95)00021-w)
- Paolo, F. S., Fricker, H. A., & Padman, L. (2015). Volume loss from Antarctic ice shelves is accelerating. *Science*, *348*(6232), 327–331. <https://doi.org/10.1126/science.aaa0940>
- Parkinson, C. L. (2019). A 40-y record reveals gradual Antarctic sea ice increases followed by decreases at rates far exceeding the rates seen in the Arctic. *Proceedings of the National Academy of Sciences*, *116*(29), 14414–14423. <https://doi.org/10.1073/pnas.1906556116>
- Patmore, R. D., Holland, P. R., Munday, D. R., Naveira Garabato, A. C., Stevens, D. P., & Meredith, M. P. (2019). Topographic control of Southern Ocean gyres and the Antarctic Circumpolar Current: A barotropic perspective. *Journal of Physical Oceanography*, *49*(12), 3221–3244. <https://doi.org/10.1175/JPO-D-19-0083.1>
- Purich, A., & England, M. H. (2021). Historical and future projected warming of Antarctic Shelf Bottom Water in CMIP6 models. *Geophysical Research Letters*, *48*(10), e2021GL092752. <https://doi.org/10.1029/2021GL092752>
- Raphael, M. N., & Hancock, M. S. (2022). A new record minimum for Antarctic sea ice. *Nature Reviews Earth & Environment*, *3*(4), 215–216. <https://doi.org/10.1038/s43017-022-00281-0>
- Raphael, M. N., Marshall, G. J., Turner, J., Fogt, R. L., Schneider, D., Dixon, D. A., et al. (2016). The Amundsen Sea low: Variability, change, and impact on Antarctic climate. *Bulletin of the American Meteorological Society*, *97*(1), 111–121. <https://doi.org/10.1175/BAMS-D-14-00018.1>
- Riahi, K., van Vuuren, D. P., Kriegler, E., Edmonds, J., O’Neill, B. C., Fujimori, S., et al. (2017). The Shared Socioeconomic Pathways and their energy, land use, and greenhouse gas emissions implications: An overview. *Global Environmental Change*, *42*, 153–168. <https://doi.org/10.1016/j.gloenvcha.2016.05.009>
- Rickard, G. J., Roberts, M. J., Williams, M. J., Dunn, A., & Smith, M. H. (2010). Mean circulation and hydrography in the Ross Sea sector, Southern Ocean: Representation in numerical models. *Antarctic Science*, *22*(5), 533–558. <https://doi.org/10.1017/S0954102010000246>
- Roach, L. A., Dörr, J., Holmes, C. R., Massonnet, F., Blockley, E. W., Notz, D., et al. (2020). Antarctic sea ice area in CMIP6. *Geophysical Research Letters*, *47*(9), e2019GL086729. <https://doi.org/10.1029/2019GL086729>
- Schodlok, M. P., Menemenlis, D., Rignot, E., & Studinger, M. (2012). Sensitivity of the ice-shelf/ocean system to the sub-ice-shelf cavity shape measured by NASA IceBridge in Pine Island Glacier, West Antarctica. *Annals of Glaciology*, *53*(60), 156–162. <https://doi.org/10.3189/2012AoG60A073>
- Sellar, A. A., Jones, C. G., Mulcahy, J. P., Tang, Y., Yool, A., Wiltshire, A., et al. (2019). UKESM1: Description and evaluation of the U.K. Earth System Model. *Journal of Advances in Modeling Earth Systems*, *11*(12), 4513–4558. <https://doi.org/10.1029/2019MS001739>
- Sellar, A. A., Walton, J., Jones, C. G., Wood, R., Abraham, N. L., Andrejczuk, M., et al. (2020). Implementation of U.K. Earth system models for CMIP6. *Journal of Advances in Modeling Earth Systems*, *12*(4), e2019MS001946. <https://doi.org/10.1029/2019MS001946>
- Shepherd, A., Ivins, E., Rignot, E., Smith, B., van den Broeke, M., Velicogna, I., et al. (2018). Mass balance of the Antarctic Ice Sheet from 1992 to 2017. *Nature*, *558*(6232), 219–222. <https://doi.org/10.1038/s41586-018-0179-y>
- Shu, Q., Wang, Q., Song, Z., Qiao, F., Zhao, J., Chu, M., & Li, X. (2020). Assessment of sea ice extent in CMIP6 with comparison to observations and CMIP5. *Geophysical Research Letters*, *47*(9), e2020GL087965. <https://doi.org/10.1029/2020GL087965>
- Siahaan, A., Smith, R., Holland, P., Jenkins, A., Gregory, J. M., Lee, V., et al. (2021). The Antarctic contribution to 21st century sea-level rise predicted by the UK Earth System Model with an interactive ice sheet. *The Cryosphere Discussions*, *2021*, 1–42. <https://doi.org/10.5194/tc-2021-371>
- Sokolov, S., & Rintoul, S. R. (2009). Circumpolar structure and distribution of the Antarctic Circumpolar Current fronts: 2. Variability and relationship to Sea Surface height. *Journal of Geophysical Research*, *114*(C11), C11019. <https://doi.org/10.1029/2008JC005248>
- Thoma, M., Jenkins, A., Holland, D., & Jacobs, S. (2008). Modelling Circumpolar Deep Water intrusions on the Amundsen Sea continental shelf, Antarctica. *Geophysical Research Letters*, *35*(18), L18602. <https://doi.org/10.1029/2008GL034939>
- Thompson, A. F., Speer, K. G., & Schulze Chretien, L. M. (2020). Genesis of the Antarctic slope current in West Antarctica. *Geophysical Research Letters*, *47*(16), e2020GL087802. <https://doi.org/10.1029/2020GL087802>
- Turner, J., Phillips, T., Hosking, J. S., Marshall, G. J., & Orr, A. (2013). The Amundsen Sea Low. *International Journal of Climatology*, *33*(7), 1818–1829. <https://doi.org/10.1002/joc.3558>
- Turner, J., Phillips, T., Marshall, G. J., Hosking, J. S., Pope, J. O., Bracegirdle, T. J., & Deb, P. (2017). Unprecedented springtime retreat of Antarctic sea ice in 2016. *Geophysical Research Letters*, *44*(13), 6868–6875. <https://doi.org/10.1002/2017GL073656>

- UKESM. (2022). United Kingdom Earth System Modelling (UKESM). 22 Denember 2022. Retrieved from <https://ukesm.ac.uk/portfolio-item/introducing-ukesm1-1-a-new-configuration-of-the-ukesm-model-with-an-improved-historical-temperature-record/>
- Walker, D. P., Jenkins, A., Assmann, K. M., Shoosmith, D. R., & Brandon, M. A. (2013). Oceanographic observations at the shelf break of the Amundsen Sea, Antarctica. *Journal of Geophysical Research: Oceans*, *118*(6), 2906–2918. <https://doi.org/10.1002/jgrc.20212>
- Wang, Z., & Meredith, M. P. (2008). Density-driven Southern Hemisphere subpolar gyres in coupled climate models. *Geophysical Research Letters*, *35*(14), L14608. <https://doi.org/10.1029/2008GL034344>
- Wang, Z., Turner, J., Wu, Y., & Liu, C. (2019). Rapid decline of total Antarctic sea ice extent during 2014–16 controlled by wind-driven sea ice drift. *Journal of Climate*, *32*(17), 5381–5395. <https://doi.org/10.1175/JCLI-D-18-0635.1>
- WOA. (2018). World Ocean Atlas 2018. [Dataset]. National Centers for Environmental Information. Retrieved from <https://www.ncei.noaa.gov/access/world-ocean-atlas-2018>